Mantle subducting slab structure in the region of the 2010 M8.8 Maule earthquake (30–40°S), Chile

J. D. Pesicek,[1] E. R. Engdahl,[2] C. H. Thurber,[1] H. R. DeShon[3] and D. Lange[4]

[1]*Department of Geoscience, University of Wisconsin-Madison, 1215 W Dayton St., Madison, WI 53706, USA. E-mail: pesicek@geology.wisc.edu*
[2]*Department of Physics, University of Colorado, Campus Box 390, Boulder, CO 80309, USA*
[3]*Center for Earthquake Research and Information, University of Memphis, 3890 Central Ave., Memphis, TN 38152, USA*
[4]*Institute of Earth and Environmental Science, University of Potsdam, Karl-Liebknecht-Str. 24-25, 14476 Potsdam-Golm, Germany*

SUMMARY

We present a new tomographic model of the mantle in the area of the 2010 M8.8 Maule earthquake and surrounding regions. Increased ray coverage provided by the aftershock data allows us to image the detailed subducting slab structure in the mantle, from the region of flat slab subduction north of the Maule rupture to the area of overlapping rupture between the 1960 M9.5 and the 2010 M8.8 events to the south. We have combined teleseismic primary and depth phase arrivals with available local arrivals to better constrain the teleseismic earthquake locations in the region, which we use to conduct nested regional–global tomography. The new model reveals the detailed structure of the flat slab and its transition to a more moderately dipping slab in the Maule region. South of the Maule region, a steeply dipping relic slab is imaged from ∼200 to 1000 km depth that is distinct from the moderately dipping slab above it and from the more northerly slab at similar depths. We interpret the images as revealing both horizontal and vertical tearing of the slab at ∼38°S to explain the imaged pattern of slab anomalies in the southern portion of the model. In contrast, the transition from a horizontal to moderately subducting slab in the northern portion of the model is imaged as a continuous slab bend. We speculate that the tearing was most likely facilitated by a fracture zone in the downgoing plate or alternatively by a continental scale terrane boundary in the overriding plate.

Key words: Seismicity and tectonics; Seismic tomography; Subduction zone processes.

1 INTRODUCTION

On 2010 February 27, an M_w 8.8 earthquake ruptured the megathrust plate interface in the Maule and Bio–Bio regions of central Chile. The rupture expanded bilaterally from the hypocentre covering ∼600 km in the region between 34° and 38°S (e.g. Delouis *et al.* 2010) and initiating an extensive aftershock sequence that exceeded the N and S limits of the coseismic rupture (Lange *et al.* 2012). The rupture zone and aftershock activity towards the south overlap with the northern limit of rupture during the 1960 M_w 9.5 great Chilean earthquake, the largest earthquake ever recorded (Cifuentes 1989). Before the 2010 Maule rupture, the region was identified as a seismic gap due to the sparse seismicity observed teleseismically (Engdahl & Villaseñor 2002) and its strong coupling observed by GPS (Ruegg *et al.* 2009). This lack of background seismicity has limited seismic investigations of the large-scale plate boundary structure and has resulted in poor resolution of global tomography models in this region (e.g. Grand *et al.* 1997; Li *et al.* 2008). In contrast, regions north of the 2010 Maule earthquake have been much more seismically active in recent times and are much better represented in global cat-

alogues, which has led to better understanding of tectonics in these areas. In particular, the region of flat slab subduction directly north of the 2010 rupture zone has been the subject of numerous regional and teleseismic studies (e.g. Cahill & Isacks 1992; Gutscher *et al.* 2000, 2002; Wagner *et al.* 2005; Anderson *et al.* 2007). As a result of the 2010 aftershock sequence, there is now an abundance of moderate and large magnitude events in the Maule region, recorded on the ever-increasing network of global seismic stations. In this study, we exploit these new teleseismically observed earthquakes to conduct a detailed tomographic investigation of the subduction zone structure along the Central Chilean margin, from the flat slab region north of Maule to the region of overlapping rupture between the 1960 and 2010 events farther south (Fig. 1).

2 EARTHQUAKE DATA AND RELOCATION

We reprocessed teleseismic data for 2605 catalogued earthquakes in the Maule region recorded by the International Seismological Centre (ISC) and National Earthquake Information Center (NEIC)
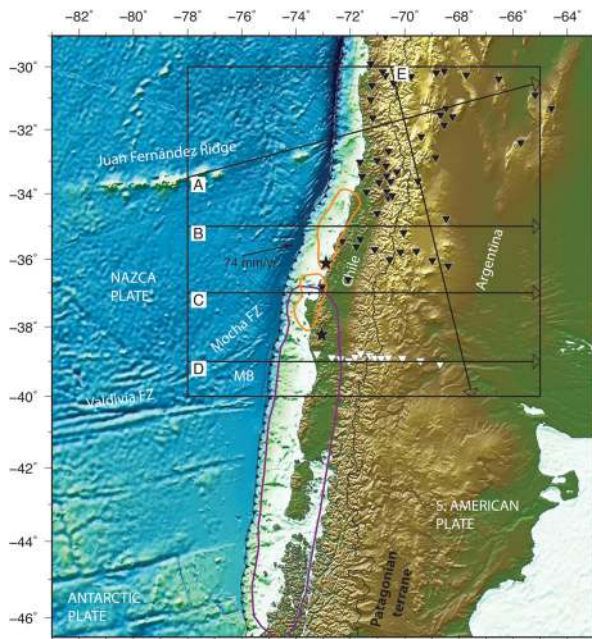
Figure 1. Map of study region. The inset box shows the boundaries of the nested regional tomography model. Convergence rate (DeMets *et al.* 2010), fracture zones (FZ) discussed in text and cross-section locations for Fig. 3 are also shown. Rupture patches with at least 5 m of slip during the 2010 *M*8.8 earthquake are shown in orange (Lorito *et al.* 2011). The extent of rupture in the 1960 *M*9.5 event is shown in dark magenta (Moreno *et al.* 2009). Black stars show the epicenters of the 1960 and 2010 events. Stations from CHARGE (Wagner *et al.* 2005) are shown as black inverted triangles. Stations used by Yuan *et al.* (2006) are shown as white inverted triangles.

for the time period 1960 February 11–2010 September 9 using the Engdahl, van der Hilst, and Buland (EHB) single event relocation method (Engdahl *et al.* 1998). To improve event location accuracy, we obtained and included additional phases in the relocation procedure from several sources. We included an additional 1255 P-phases for 47 events from several local deployments before the 2010 Maule rupture (Campos *et al.* 2002; Wagner *et al.* 2005; Haberland *et al.* 2006; Anderson *et al.* 2007). For aftershocks, we included 4977 P-phases from 267 stronger events recorded by the international maule aftershock data set (IMAD) network (Lange *et al.* 2012). To better constrain focal depth, we also included 3839 reported depth phases (pP, sP and pwP) that until recently were not used routinely by global location agencies. The combined catalogue of phase data was then reprocessed using the EHB method. This method employs a variety of strategies to increase the accuracy of the teleseismic locations, including iterative relocation with dynamic phase identification, phase-weighting as a function of model uncertainty variance with epicentral distance, and ellipticity and station patch corrections. The new locations are shown in Fig. S1.

3 TOMOGRAPHY METHOD

We applied the nested regional–global tomographic method of Pesicek *et al.* (2008; 2010), based on the work of Widiyantoro & van der Hilst (1996) to this combined data set. The regional model domain is parametrized into $0.5° \times 0.5°$ constant slowness cells with cell thickness increasing with depth from 35 km in the uppermost layer to 110 km at the base of the regional model at 1600 km. The regional model is embedded in a coarser ($5° \times 5°$) global model

that extends to 2889 km depth with an average layer thickness of ~180 km. Outside the regional model, we traced geometric rays through the global 3-D model MITP08 (Li *et al.* 2008), which we adapted to fit our coarse regular parametrization. Inside the regional model, we traced rays through the spherically symmetric global model ak135 (Kennett *et al.* 1995), but with two modifications. First, we incorporated crustal heterogeneity into the top layer using the CRUST 2.0 global model (Bassin *et al.* 2000). Second, we increased the average radial velocity below the crustal layer by 0.5 per cent. Our initial results showed widespread high-velocity perturbations to ak135 on the order of 0.5 per cent in all well-sampled mantle regions of the model, which suggests that a corresponding increase in the reference model velocity better represents average velocity structure in the region. Using the modified reference model, we computed traveltime residuals and inverted arrival residuals of 6 s or less. We performed a linear inversion using the LSQR algorithm (Paige & Saunders 1982). Damping and smoothing coefficients were chosen by examining the trade-off between data and model variance and by examining the results of synthetic restorations tests of both short- and long-wavelength features (Figs S2–S5). Twice as much damping was applied to the crustal layer to prevent smearing of poorly resolved crustal anomalies into the upper mantle.

To further increase upper mantle ray sampling, we also included data for additional events located by the CHARGE array (Wagner *et al.* 2005; Anderson *et al.* 2007; Figs 1 and S1). Many of the events located by these stations sample the upper mantle in the study region. In addition, we included P-phases for 52 teleseismic events recorded by the ISSA array at ~39°S (Yuan *et al.* 2006; Fig. 1). We have not included the smaller magnitude local events located by other networks with smaller apertures (e.g. Lange *et al.* 2012), due to their limited mantle sampling.

4 RESULTS AND DISCUSSION

The model results are shown in Figs 2 and 3. As the LSQR inversion is an approximate technique, formal resolution is not computed. To judge and illustrate the resolution of the model, we have compared the results of restoration tests (Figs S2–S5) to ray density maps (Fig. S6) to choose a ray sampling threshold above which synthetic anomalies are well restored. The comparison suggests that cells with total ray lengths exceeding ~3000 km are well resolved. Throughout most of the model domain, this level of sampling occurs to depths of ~900 km and in some areas up to 1200 km depth, as indicated in Figs 2 and 3.

Several well-resolved features are illuminated in the new model. In the northern portion of the model, the flat slab is well defined by the hypocentre relocations and coincident fast velocities. Above the flat slab, a large prominent low-velocity region is also apparent. South of the flat slab, the dip angle of the imaged subducting slab becomes more moderate. Previous workers have suggested that the transition from flat to normal subduction in this region might be accommodated by a slab tear in seismically active portions of the slab (Cahill & Isacks 1992). However, a profile perpendicular to the subducting Juan Fernández (JF) Ridge (Fig. 3e) shows the continuity and broad curvature of the slab between the regions of flat versus moderate subduction (*cf*. Figs 3a and b). Thus, our results suggest that slab bending rather than tearing accommodates this transition in dip. Farther inboard, east of 67°W, in the aseismic portion of the slab, there may be a local tear between the horizontal and normally dipping sections of the slab. On the basis of discrepant *T*-axes orientations, Anderson *et al.* (2007) suggest that a local slab tear

may exist in the vicinity of 66°W, 32°S below ~150 km depth. Our model shows a gap in the high velocities at this location from depths of 220 to 340 km (Fig. 2, labelled A at 220–280 km depth) and thus supports such an interpretation.

Flat slab subduction north of ~32°S has been attributed by many authors to subduction of the JF Ridge (e.g. Yáñez *et al.* 2001). The JF Ridge traces the westward track of the JF hotspot to its current location at ~82°W (Fig. 1; von Huene *et al.* 1997). We clearly image a region of reduced velocities at depths of 500–1000 km that is spatially coincident with the JF Ridge at the surface (Figs 2 and 3a). Centered at ~33°S, 77°W, this anomaly is located well east of the plume imaged by Montelli *et al.* (2004) at similar depths, which is centred farther west at ~90°W and evidently does not extend east of 80°W. However, Zhao (2007) shows a much broader and laterally extensive slow zone beneath the JF hotspot at these depths, which in his model extends eastwards all the way to the plate boundary. We cannot image the western extent of the JF plume, but our results also suggest that it does extend as far east as 74°W (Figs 2 and 3a).

South of the subducting JF Ridge and the flat slab, we clearly image a continuous fast slab throughout the region that ruptured in the 2010 M_w 8.8 event, with a dip of ~30° that agrees well with the dip angle defined by slab seismicity (Figs 3b and c) and inferred from arc magma chemistry (Kay *et al.* 2006a,b). The slab in this region maintains a constant dip throughout the upper mantle and penetrates the transition zone with little apparent deflection before exiting the model east of 65°W.

South of the Maule rupture zone (~38–40°S), a distinct change in the pattern of fast anomalies is observed. In this region, a continuous, moderately dipping slab throughout the upper mantle (e.g. Figs 3b and c) is no longer evident. Instead, the shallow expression of the moderately dipping slab ends at ~200 km depth, at roughly the same point as the limit of intermediate depth slab seismicity (Fig. 3d). Below and west of the seismically active slab, a steeply dipping fast anomaly is imaged from ~200 km depth throughout the transition zone and into the lower mantle. This feature is high in amplitude and markedly different from the deeper slab farther north of ~38°S (*cf*. Figs 3b–d). Although seismicity (Fig. S1) and ray density (Fig. S6) in general decrease towards the south, ray density is still high in this area and expands with depth. We are able to recover synthetic anomalies quite well in this region (Figs S2–S5). The reduction in ray density does have the affect of slightly decreasing the amplitudes of the restored anomalies in the southernmost portion of the model. But the relative strength of the southern anomaly in the real model compared to more northerly regions, despite the decrease in ray density, suggests that this feature is robust and that the velocities may even be higher than those to the north.
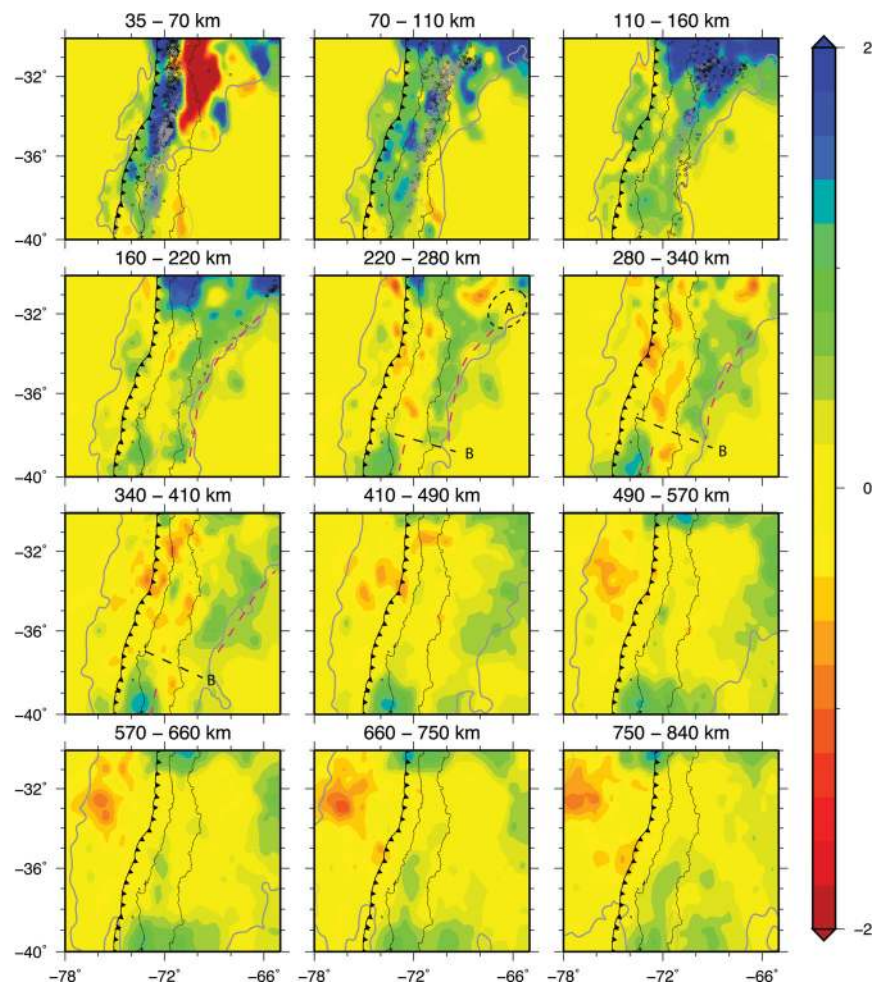

Figure 2. Map slices through the tomography model (shown as per cent perturbation to the reference model). Relocated EHB seismicity is shown as black circles and other locations from local deployments shown as grey circles. Grey contours encircle well-resolved regions as discussed in text. The black ellipse labelled A at 220–280 shows the location a slab tear as hypothesized by Anderson *et al.* (2007). The leading edge of the inferred slab (dashed magenta line) and the interpreted vertical slab tear (black dashed line labelled B) are shown at several depths.
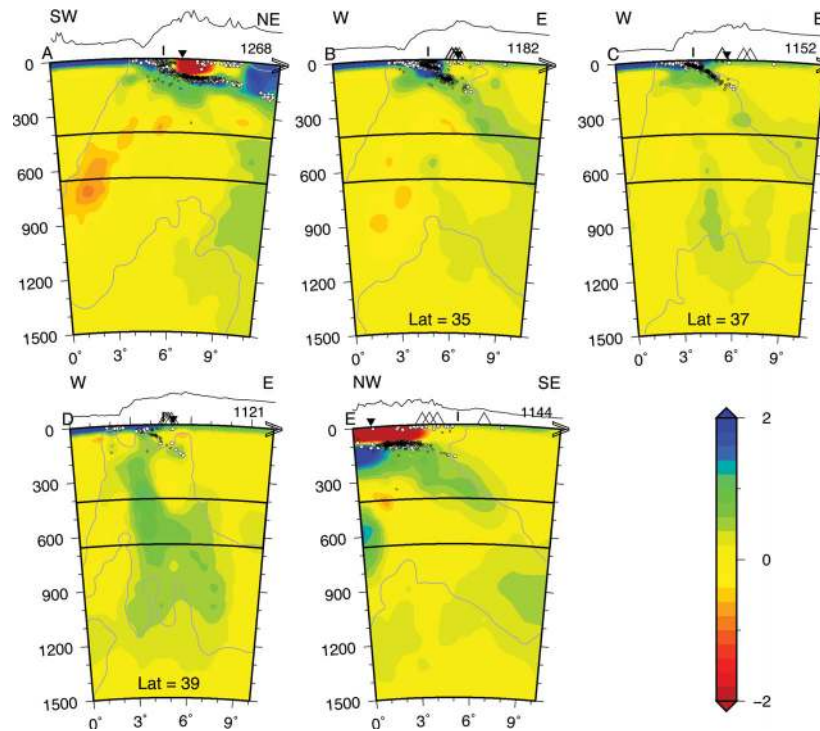
Figure 3. Vertical cross-sections through tomography model (locations shown in Fig. 1) shown as perturbations to the reference model in percent. Relocated EHB locations are shown in white and other locations from local deployments are shown in black. Approximated resolution contours are shown in grey as discussed in text. Triangles at surface show volcano locations whereas vertical lines and inverted triangles show the locations of the coastline and international border, respectively. Cross-section lengths in km are shown at the top right of each section. Exaggerated topography (20×) is also shown. The cross-section locations highlight (a) flat slab subduction and the Juan Fernández (JF) ridge, (b and c) normal subduction in the Maule region with a moderate dip (~30°), (d) slab tearing and detachment at ~200 km depth at 39°S and (e) slab bending representing the transition from moderate to flat slab subduction to the north.

The fast velocities at ~39°S reveal a first order slab feature in the mid-mantle not visible in previous tomography studies with sparser sampling in this region (e.g. Li *et al.* 2008). We suggest that the geometry of this feature represents both vertical tearing of the slab at ~38°S and horizontal detachment of a relic slab now at ~200 km depth. Fig. 2 shows that the slab below 200 km depth does not curve gently to accommodate the steeper dip to the south as it does farther north in the transition from flat to moderate dip (Fig. 3e). Rather, the images show that a significant gap exists at ~38°S between the moderately dipping slab to the north and the steeply dipping feature to the south that we interpret as a vertical tear (Fig. 2, labelled B, 220–410 km). In fact, slow anomalies separate the two distinct slabs segments in this region, highlighting the slab separation below ~200 km depth.

At ~39°S, the fast slab dips at ~30° to depths of ~200 km beneath the volcanic arc, in good agreement with our relocated hypocentres (Fig. 3d). Other studies confirm that this dip angle is constant at similar depths from 38 to 43°S (Haberland *et al.* 2006; Lange *et al.* 2007) but may increase to ~50° from 44 to 45°S (R. Russo, personal communication 2012). Below 200 km depth, the slab feature locates farther west, beneath the trench and continues in the lower mantle with a steep dip. Although this western anomaly appears connected to the shallower seismically active segment (Fig. 3d), this seems physically implausible and we attribute the apparent connection to vertical smearing of the two anomalies (Fig. S5). The location of the top of the relic slab beneath the trench and the bottom of the seismically active slab farther east at the same depth (~200 km) suggest that these two anomalies may have the same origin at the plate boundary and previously comprised a single

segment that detached along a horizontal tear. The proximity of the deep segment to the trench and the opposing dip of the shallow segment suggest that the horizontal tear may have initiated near the surface. This may have occurred in the fashion envisaged by Toda *et al.* (2008), who suggest that subducted outer-rise normal faulting might have facilitated shallow slab fragmentation beneath Tokyo. The location of the end of the tear and the continuity of the relic slab feature to the south is an open question. We speculate that the horizontal tear ends and a contiguous slab resumes again at 44–45°S, where a steeper dip of ~50° is observed.

Insight into the slab tearing and detachment in the region might be explained within the context of the tectonic history of subduction in the region. The convergent plate boundary along the west coast of South America is the result of the complex tectonics in the Pacific basin resulting primarily from spreading between the Pacific, Antarctic, Phoenix (or Aluk) and Farallon plates since at least 84 Ma (Zonenshayn *et al.* 1984; Cande & Leslie 1986). The ridge system between the Farallon and Phoenix plates began subducting beneath South America at ~63 Ma, though its latitudinal intersection along the South American trench is still debated (Cande & Leslie 1986; Breitsprecher & Thorkelson 2009 and references therein). At 26–27 Ma, the Farallon Plate segmented into the Nazca and Cocos plates but spreading continued between the Nazca and Phoenix plates and subduction of the ridge system beneath South American continued. By 18 Ma, the triple junction between the Nazca, Phoenix and Antarctic plates began subducting beneath South America, forming a quadruple plate junction (Breitsprecher & Thorkelson 2009). By ~10 Ma, the Nazca–Phoenix spreading system had completely subducted, leaving only the Nazca–Antarctic junction that continues

to subduct beneath Patagonia today, forming a well-known slab window (e.g. Breitsprecher & Thorkelson 2009; Russo *et al.* 2010).

To reconcile the tectonic history of the region with our imaged slab, we bracketed the time period of subduction of the Nazca slab in the Maule region, which we image as a continuous feature from the surface into the transition zone at least as far east as our model boundary at 65°W (Figs 3b and c). The rate of palaeo-convergence between the Nazca and South America plates for the period 25–5 Ma is ∼100 mm yr^{-1} in the ENE direction (Cande & Leslie 1986), which is higher than the modern rate of ∼74 mm yr^{-1} in the same direction (DeMets *et al.* 2010). Considering these two subduction rates and a slab length of 800 km (74–65°W at 36°S), the slab imaged in our model must have subducted within the last ∼8–10 Ma. This age agrees with what Grand (1994) suggests for the age of mid-mantle slab farther north. This simple calculation excludes the relic Phoenix Plate and its spreading boundary as being related to the torn slab. By 8 Ma, the Nazca–Phoenix spreading ridge had long since subducted and the triple junction between the Nazca–Antarctic spreading ridge and the South American plate was located too far south (∼48°S) to influence subduction in our study region (Breitsprecher & Thorkelson 2009). Thus, the slab geometry we have imaged must have formed during the constant ENE-directed subduction of the Nazca plate in the past ∼8–10 Ma. If the mid-mantle slab began subducting at ∼8–10 Ma, the horizontal slab detachment at ∼200 km depth must have occurred more recently. The ∼350 km of slab from 0 to 200 km depth suggests that the seismically active, moderately dipping slab segment subducted within the last ∼3–5 Ma.

Several geologic studies have attempted to explain the subduction history in this region occurring over the past ∼11 Ma and earlier based on variations of volcanic rock chemistry. These studies suggest that a transition from shallow to moderate slab subduction occurred at ∼5 Ma in the region from ∼35 to 38°S (Kay *et al.* 2006a,b; Ramos & Kay 2006; Ramos & Folguera 2009; Folguera & Ramos 2011). In contrast, a stable magmatic arc and constant slab dip existed directly south of this area at this time, though the arc has narrowed more recently (Lara & Folguera 2006). Thus, the available geochemical data [and also structural data (Folguera *et al.* 2006)] suggest different slab histories north and south of ∼38°S, consistent with our vertical tear interpretation. However, we have found no evidence of any magmatic hiatus south of 38°S at this time as might be expected from a horizontal slab detachment event. The limited geochronologic data at ∼5 Ma in this region currently prevent a more detailed investigation of arc chemistry in relation to the slab features in our model.

An obvious candidate for explaining the slab tearing and detachment might be the subduction of a spreading ridge and the resulting slab window. However, we have shown that this scenario is unlikely in this region. Thus, an alternative explanation must be sought. We suggest that relic features of the upper and/or lower plate have influenced slab segmentation. At the latitude of the inferred vertical slab tear, there is a pervasive, continent-wide terrane boundary that extends eastwards into the Atlantic Ocean basin. This boundary records the collision of the Patagonian terrane with Gondwana in the Paleozoic and separates an area of active Neogene compression to the north from a region with structures formed earlier in the Cretaceous to the south (Chernicoff & Zappettini 2004; Melnick *et al.* 2009). It is conceivable that large-scale differences in the overriding lithosphere may have induced stress heterogeneities in the slab that eventually led to tearing.

Additionally, many authors have noted the different origin of the subducting oceanic crust north and south of the Mocha and
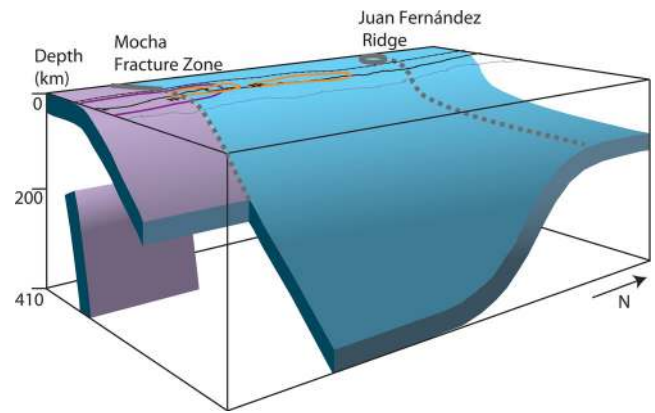

Figure 4. Schematic block diagram illustrating interpreted slab geometry in the upper mantle. Slip patches, 1960 and 2010 epicentres and other features from Fig. 1 are also shown.

Valdivia fracture zones, respectively. These fracture zones (FZs), which are readily visible in bathymetric (Fig. 1) and geopotential data, form a triangular region with the Chile trench, referred to as the Mocha Block, that represents a fundamental tectonic boundary (e.g. Melnick *et al.* 2009; Contreras-Reyes *et al.* 2010). North of the Mocha Block, old (30–35 Ma) oceanic lithosphere originating from spreading of the Pacific and Nazca plates along the East Pacific Rise is subducting. South of it, younger (0–25 Ma) oceanic lithosphere that originated along the Chile Rise via spreading between the Nazca and Antarctic plates is subducting (Tebbens & Cande 1997). Thus, this region marks a transition in oceanic plate age and thickness that could be manifested as a significant structural weakness at depth. A tear developing in response to stresses in the slab could exploit this weakness. This scenario is analogous to subduction at the northern end of the Nazca plate where the Carnegie Ridge collides with the North Andean margin. In this region, a slab tear occurs along the Grijalva FZ, which separates Farallon oceanic crust from younger Cocos–Nazca crust (Gutscher *et al.* 1999).

Our preferred interpretation of the imaged slab geometry (Fig. 4) is one where the vertical slab tear initiated and developed along the Mocha FZ whereas the horizontal slab tear initiated close to the surface, possibly along an outer-rise normal fault. The resulting slab segment began sinking into the mantle beneath the trench as subduction resumed. However, there are two potential issues with this interpretation. One is the position of the slab segment relative to S. American plate, which is moving westward relative to the mantle in a hotspot reference frame (HS3-NUVEL1A; Gripp & Gordon 2002). The ∼45 ± 5 mm yr^{-1} of westward motion of S. America relative to the mantle since the hypothesized detachment at ∼3–5 Ma suggests westward motion of the trench since detachment at the surface in the ∼120–250 km range. But the near vertical slab segment we imaged (Fig. 3d) still appears largely beneath the trench rather than east of it as might be expected. We estimate that there is only ∼100 km of offset between the current trench position and the approximate surface detachment point of the segment. Although this simple calculation reveals a potential minor discrepancy, we do not consider it significant enough to negate our general interpretation given our inability to precisely locate the position and boundaries of slab features in the tomographic model and the lack of other explanations for the large robust mantle feature imaged south of ∼38°S.

A second issue concerns the younging of the oceanic crust toward the south and how this affects the thermal thickness of the slab imaged by tomography. An alternative explanation of our model

is that we simply lose the ability to image the slab farther south due to decreasing thermal thickness and/or ray coverage. Fig. 3(d) shows that the high velocity, seismically active, moderately dipping slab ends at ∼200 km depth. To the east of the slab seismicity, resolution diminishes whereas farther north in this same region resolution is better and the moderately dipping slab is imaged well into the transition zone. Thus, it is fair to question whether we would be able to image the continuation of the moderately dipping slab below ∼200 km depth at ∼38° and southwards. Even with sufficient resolution in this region, we expect the younger slab to have a smaller thermal thickness and thus be more difficult to image than areas to the north. Based on oceanic crustal ages and density modelling, Tassara *et al.* (2006) show a variation of ∼15 km in the lithospheric thickness across our model region, from 75–90 km at 30°S to 60–75 km at 40°S.

To address these potential issues, we conducted additional synthetic slab tests at 39°S to determine whether or not the missing extension of the moderately dipping slab beneath ∼200 km depth is a result of poor resolution and/or decreased thermal slab thickness. Fig. S7 shows the results of two additional slab tests where the synthetic slab dips moderately throughout the upper mantle and into the transition zone with thicknesses of ∼67 and ∼33 km, respectively (compared to ∼177 km for the slab in Fig. S5). These tests show that a lithospheric slab with thickness ∼67 km or greater will readily be imaged with tomography, even outside of our conservatively chosen resolution contour (Fig. S7b). In comparison, a ∼33-km-thick slab, which is much thinner than realistic estimates (Tassara *et al.* 2006), is more difficult to image (Fig. S7d) but would still be visible in our model (Fig. S7f). Thus, we are confident that we would image such slab geometry if it existed. These results, and the fast anomalies in the real model (Figs 2, 3d and S7e) all suggest that the shallow, moderately dipping slab ends at ∼200 km depth and is detached from the deeper near vertical relic slab below it.

5 CONCLUSION

We have presented a new tomographic model of the mantle beneath the Maule and adjacent regions in Chile based on an updated catalogue of teleseismic earthquake data including arrival time data from temporary local networks. The dense aftershock seismicity for the first time allows detailed imaging of the subducting slab at upper- and mid-mantle depths along the central portion of the Chilean subduction zone. The geometry of the subducting slab in the mantle shows a variety of subduction styles in the region, broadly illustrating the transition from flat slab subduction in the north to steep slab subduction in the south. Gentle slab bending accommodates the transition from flat slab subduction in the north to normal subduction in the center of the model along the Maule 2010 rupture zone. In the southern portion of the model, we imaged a region with elevated velocities that we interpret as a detached slab fragment at depths below ∼200 km that dips steeply and appears disconnected from the normally subducting slab above it. We suggest that this feature represents tearing and detachment of the slab (Fig. 4). The reason for slab tearing in the south, in contrast to gentle bending in the north, is uncertain but could be related to relic features within the overriding or downgoing plates.

ACKNOWLEDGMENTS

REFERENCES

Anderson, M., Alvarado, P., Zandt, G. & Beck, S., 2007. Geometry and brittle deformation of the subducting Nazca Plate, central Chile and Argentina, *Geophys. J. Int.,* **171**(1), 419–434, doi:10.1111/j.1365-246X.2007.03483.x.

Bassin, C., Laske, G. & Masters, G., 2000. The current limits of resolution for surface wave tomography in North America, *EOS, Trans. Am. geophys. Un.,* **81,** F897.

Breitsprecher, K. & Thorkelson, D.J., 2009. Neogene kinematic history of Nazca–Antarctic–Phoenix slab windows beneath Patagonia and the Antarctic Peninsula, *Tectonophysics,* **464**(1–4), 10–20, doi:10.1016/j.tecto.2008.02.013.

Cahill, T.A. & Isacks, B.L., 1992. Seismicity and shape of the subducted Nazca Plate, *J. geophys. Res,* **97**(B12), 17–17 529, doi:10.1029/92JB00493.

Campos, J. *et al.*, 2002. A seismological study of the 1835 seismic gap in south-central Chile; Subduction zone structure and megathrust earthquakes, *Phys. Earth planet. Inter.,* **132,** 177–195.

Cande, S.C. & Leslie, R.B., 1986. Late Cenozoic Tectonics of the Southern Chile Trench, *J. geophys. Res.,* **91,** 471–496, doi:10.1029/JB091iB01p00471.

Cifuentes, I.L., 1989. The 1960 Chilean Earthquakes, *J. geophys. Res.,* **94**(B1), 665–680.

Chernicoff, C.J. & Zappettini, E.O., 2004. Geophysical Evidence for Terrane Boundaries in South-Central Argentina, *Gondwana Res.,* **7**(4), 1105–1116, doi:10.1016/S1342-937X(05)71087-X.

Contreras-Reyes, E., Flueh, E.R. & Grevemeyer, I., 2010. Tectonic control on sediment accretion and subduction off south central Chile: Implications for coseismic rupture processes of the 1960 and 2010 megathrust earthquakes, *Tectonics,* **29**(6), TC6018, doi:10.1029/2010TC002734.

Delouis, B., Nocquet, J. & Vallee, M., 2010. Slip distribution of the February 27, 2010 Mw = 8.8 Maule earthquake, central Chile, from static and high-rate GPS, InSAR, and broadband teleseismic data, *Geophys. Res. Lett.,* **37**(17), L17305, doi:10.1029/2010GL043899.

DeMets, C., Gordon, R.G. & Argus, D.F., 2010. Geologically current plate motions, *Geophys. J. Int,* **181**(1), 1–80, doi:10.1111/j.1365-246X.2009.04491.x.

Engdahl, E.R. & Villaseñor, A., 2002. Global seismicity: 1900–1999, in *International Handbook of Earthquake and Engineering Seismology, Part A*, Chapter 41, pp. 665–690, eds Lee, W.H.K., Kanamori, H., Jennings, P.C. & Kisslinger, C., Academic Press, Amsterdam.

Engdahl, E.R., van der Hilst, R.D. & Buland, R., 1998. Global teleseismic earthquake relocation with improved travel times and procedures for depth determination, *Bull. seism. Soc. Am.,* **88,** 722–743.

Folguera, A., Zapata, T. & Ramos, V.A., 2006. Late Cenozoic extension and the evolution of the Neuquén Andes, *Geol. Soc. Am. Special Papers,* **407,** 267–285, doi:10.1130/2006.2407(12).

Folguera, A. & Ramos, V.A., 2011. Repeated eastward shifts of arc magmatism in the Southern Andes: a revision to the long-term pattern of Andean uplift and magmatism, *J. S. Am. Earth Sci.,* **32**(4), 531–546, doi:10.1016/j.jsames.2011.04.003.

Grand, S.P., 1994. Mantle shear structure beneath the Americas and surrounding oceans, *J. geophys. Res.,* **99,** 11 591–11 621, doi:10.1029/94JB00042.

Grand, S.P., van der Hilst, R.D. & Widiyantoro, S., 1997. Global seismic tomography; a snapshot of convection in the Earth, *GSA Today,* **7**(4), 1–7.

Gripp, A.E. & Gordon, R.G., 2002. Young tracks of hotspots and current plate velocities, *Geophys. J. Int,* **150**(2), 321–361, doi:10.1046/j.1365-246X.2002.01627.x.

Gutscher, M., 2002. Andean subduction styles and their effect on thermal structure and interplate coupling, *J. S. Amer. Earth Sci.,* **15**(1), 3–10, doi:10.1016/S0895-9811(02)00002-0.

Gutscher, M., Malavieille, J., Lallemand, S. & Collot, J., 1999. Tectonic segmentation of the North Andean margin: impact of the Carnegie Ridge collision, *Earth planet. Sci. Lett.,* **168**(3–4), 255–270, doi:10.1016/S0012-821X(99)00060-6.

Gutscher, M., Spakman, W., Bijwaard, H. & Engdahl, E.R., 2000. Geodynamics of flat subduction; seismicity and tomographic constraints from the Andean margin, *Tectonics,* **19**(5), 814–833, doi:10.1029/1999TC001152.

Haberland, C., Rietbrock, A., Lange, D., Bataille, K. & Hofmann, S., 2006. Interaction between forearc and oceanic plate at the south-central Chilean margin as seen in local seismic data, *Geophys. Res. Lett.,* **33**(23), L23302, doi:10.1029/2006GL028189.

Kay, S.M., Burns, W.M., Copeland, P. & Mancilla, O., 2006. Upper Cretaceous to Holocene magmatism and evidence for transient Miocene shallowing of the Andean subduction zone under the northern Neuquén Basin, *Geol. Soc. Am. Special Papers,* **407,** 19–60, doi:10.1130/2006.2407(02).

Kay, S.M., Mancilla, O. & Copeland, P., 2006. Evolution of the late Miocene Chachahuén volcanic complex at 37°S over a transient shallow subduction zone under the Neuquén Andes, *Geol. Soc. Am. Special Papers,* **407,** 215–246, doi:10.1130/2006.2407(10).

Kennett, B.L.N., Engdahl, E.R. & Buland, R., 1995. Constraints on seismic velocities in the Earth from traveltimes, *Geophys. J. Int.,* **122,** 108–124.

Lange, D., Rietbrock, A., Haberland, C., Bataille, K., Dahm, T., Tilmann, F. & Flüh, E.R., 2007. Seismicity and geometry of the south Chilean subduction zone (41.5°S–43.5°S): Implications for controlling parameters, *Geophys. Res. Lett.,* **34**(6), L06311, doi:10.1029/2006GL029190.

Lange, D. *et al.*, 2012. Aftershock seismicity of the 27 February 2010 Mw 8.8 Maule earthquake rupture zone, *Earth planet. Sci. Lett.,* 317–318, 413–425, doi:10.1016/j.epsl.2011.11.034.

Lara, L.E. & Folguera, A., 2006. The Pliocene to Quaternary narrowing of the Southern Andean volcanic arc between 37° and 41°S latitude, *Geol. Soc. Am. Special Papers,* **407,** 299–315, doi:10.1130/2006.2407(14).

Li, C., van der Hilst, R.D., Engdahl, E.R. & Burdick, S., 2008. A new global model for P wave speed variations in Earth's mantle, *Geochem. Geophys. Geosyst.,* **9,** 1–21.

Lorito, S. *et al.*, 2011. Limited overlap between the seismic gap and co-seismic slip of the great 2010 Chile earthquake, *Nature Geosci.,* **4**(3), 173–177.

Melnick, D., Bookhagen, B., Strecker, M.R. & Echtler, H.P., 2009. Segmentation of megathrust rupture zones from fore-arc deformation patterns over hundreds to millions of years, Arauco peninsula, Chile, *J. geophys. Res.,* **114**(B1), B01407, doi:10.1029/2008JB005788.

Montelli, R., Nolet, G., Dahlen, F.A., Masters, G., Engdahl, E.R. & Hung, S., 2004. Finite-frequency tomography reveals a variety of plumes in the mantle, *Science,* **303**(5656), 338–343, doi:10.1126/science.1092485.

Moreno, M.S., Bolte, J., Klotz, J. & Melnick, D., 2009. Impact of megathrust geometry on inversion of coseismic slip from geodetic data; application to the 1960 Chile earthquake, *Geophys. Res. Lett.,* **36**(16), doi:10.1029/2009GL039276.

Paige, C. & Saunders, M.A., 1982. LSQR: an algorithm for sparse linear equations and least squares problems, *ACM Trans. Math. Soft.,* **8,** 43–71.

Pesicek, J.D., Thurber, C.H., Widiyantoro, S., Engdahl, E.R. & Deshon, H.R., 2008. Complex slab subduction beneath northern Sumatra, *Geophys. Res. Lett.,* **35**(20), doi:10.1029/2008GL035262.

Pesicek, J.D., Thurber, C.H., Widiyantoro, S., Zhang, H., DeShon, H.R. & Engdahl, E.R., 2010. Sharpening the tomographic image of the subducting slab below Sumatra, the Andaman Islands and Burma, *Geophys. J. Int.,* **182**(1), 433–453, doi:10.1111/j.1365-246X.2010.04630.x.

Ramos, V.A. & Folguera, A., 2009. Andean flat-slab subduction through time, *Geol. Soc. Lond. Special Publ.,* **327**(1), 31–54, doi:10.1144/SP327.3.

Ramos, V.A. & Kay, S.M., 2006. Overview of the tectonic evolution of the southern Central Andes of Mendoza and Neuquén (35°–39°S latitude), *Geol. Soc. Am. Special Papers,* **407,** 1–17, doi:10.1130/2006.2407(01).

Ramos, V.A., 2000. The Southern Central Andes, 561–604 pp., In-Folo Producao Editorial, Grafica e Programacao Visual, Rio de Janeiro, Brazil.

Ruegg, J. *et al.*, 2009. Interseismic strain accumulation measured by GPS in the seismic gap between Constitución and Concepción in Chile, *Phys. Earth planet. Inter.,* **175**(1–2), 78–85. doi:10.1016/j.pepi.2008.02.015.

Russo, R. *et al.*, 2010. Subduction of the Chile Ridge: upper mantle structure and flow, *GSA Today,* **20**(9), doi:10.1130/GSATG61A.1.

Tassara, A., Götze, H.-J., Schmidt, S. & Hackney, R., 2006. Three-dimensional density model of the Nazca plate and the Andean continental margin, *J. geophys. Res.,* **111**(B9), B09404, doi:10.1029/2005JB003976.

Tebbens, S.F. & Cande, S.C., 1997. Southeast Pacific tectonic evolution from early Oligocene to present, *J. geophys. Res,* **102**(B6), 12 061–12 084, doi:10.1029/96JB02582.

Toda, S., Stein, R.S., Kirby, S.H. & Bozkurt, S.B., 2008. A slab fragment wedged under Tokyo and its tectonic and seismic implications, *Nat. Geosci.,* **1**(11), 771–776.

von Huene, R., Corvalán, J., Flueh, E.R., Hinz, K., Korstgard, J., Ranero, C.R., Weinrebe, W., CONDOR Scientists, 1997. Tectonic control of the subducting Juan Fernández Ridge on the Andean margin near Valparaiso, Chile, *Tectonics,* **16**(3), 474–488, doi:10.1029/96TC03703.

Wagner, L.S., Beck, S. & Zandt, G., 2005. Upper mantle structure in the south central Chilean subduction zone (30° to 36°S), *J. geophys. Res.,* **110**(B1), 20, doi:10.1029/2004JB003238.

Widiyantoro, S. & van der Hilst, R.D., 1996. Structure and evolution of lithospheric slab beneath the Sunda Arc, Indonesia, *Science,* **271,** 1566–1570.

Yáñez, G.A., Ranero, C., von Huene, R. & Díaz, J., 2001. Magnetic anomaly interpretation across the southern central Andes (32°–34°S): the role of the Juan Fernández Ridge in the late Tertiary evolution of the margin, *J. geophys. Res.,* **106,** 6325–6345, doi:10.1029/2000JB900337.

Yuan, X. *et al.*, 2006. Deep seismic images of the Southern Andes, *Geol. Soc. Am. Special Papers,* **407,** 61–72, doi:10.1130/2006.2407(03).

Zhao, D., 2007. Seismic images under 60 hotspots: search for mantle plumes, *Gondwana Res.,* **12**(4), 335–355, doi:10.1016/j.gr.2007.03.001.

Zonenshayn, L.P., Savostin, L.A. & Sedov, A.P., 1984. Global paleogeodynamic reconstructions for the last 160 million years, *Geotectonics,* **18**(3), 181–195.

SUPPORTING INFORMATION

Additional Supporting Information may be found in the online version of this article:

Figure S1. EHB locations (circles) and CHARGE locations (squares) for historical and aftershock events used for tomography in this study, colour-coded by depth. Black smaller circles underneath are other earthquake locations from previous local deployments (see text for references). The black earthquakes are not used for tomography but are shown here and in Figs 2 and 3 for reference. The locations of the trench and international border are shown in black.

Figure S2. Depth slices for spike restoration test. Synthetic 4 per cent velocity perturbation input anomalies ($1° \times 1°$; black contours) are separated by $1.5°$ in latitude and longitude and by two layers in depth. Depths with no input anomalies are shown as well and the perturbations in these layers are an indication of vertical smearing from adjacent layers. Other features explained in Fig. 2 caption.

Figure S3. Depth slices for alternate spike restoration test, the same as Fig. S2 except the input pattern (black contours) is shifted to be the opposite of Fig. S2, i.e. layers with (without) anomalies in Fig. S1 now lack (have) them. Other features explained in Fig. 2 caption.

Figure S4. Depth slices for restoration test for large-scale features (4 per cent velocity perturbation). The input anomalies are shown

by magenta contours in each layer. Other features explained in Fig. 2 caption.

Figure S5. Latitudinal cross-sections of restoration test for large-scale features (4 per cent velocity perturbation; see also Fig. S4). The top row shows the synthetic input anomalies and the bottom row shows their restored geometry.

Figure S6. Layer ray sampling shown as the log of the total ray length (km) for each cell.

Figure S7. Synthetic slab restoration tests designed to assess the ability of the tomography method to recover a continuous moderately dipping slab at 39°S. See also Fig. 3 caption.

Please note: Wiley-Blackwell is not responsible for the content or functionality of any supporting materials supplied by the authors. Any queries (other than missing material) should be directed to the corresponding author for the article.